

LES validation of urban flow, part II: eddy statistics and flow structures

Article

Accepted Version

Hertwig, D. ORCID: <https://orcid.org/0000-0002-2483-2675>, Patnaik, G. and Leidl, B. (2017) LES validation of urban flow, part II: eddy statistics and flow structures. *Environmental Fluid Mechanics*, 17 (3). pp. 551-578. ISSN 1567-7419 doi: 10.1007/s10652-016-9504-x Available at <https://centaur.reading.ac.uk/76908/>

It is advisable to refer to the publisher's version if you intend to cite from the work. See [Guidance on citing](#).

To link to this article DOI: <http://dx.doi.org/10.1007/s10652-016-9504-x>

Publisher: Springer

All outputs in CentAUR are protected by Intellectual Property Rights law, including copyright law. Copyright and IPR is retained by the creators or other copyright holders. Terms and conditions for use of this material are defined in the [End User Agreement](#).

www.reading.ac.uk/centaur

CentAUR

Central Archive at the University of Reading

Reading's research outputs online

1 **LES validation of urban flow, part II: eddy statistics and flow**
2 **structures**

3 **Denise Hertwig · Gopal Patnaik · Bernd Leitl**

4
5 Received: date / Accepted: date

6 **Abstract** Time-dependent three-dimensional numerical simulations such as large-eddy sim-
7 ulation (LES) play an important role in fundamental research and practical applications in
8 meteorology and wind engineering. Whether these simulations provide a sufficiently accu-
9 rate picture of the time-dependent structure of the flow, however, is often not determined in
10 enough detail.

11 We propose an application-specific validation procedure for LES that focuses on the
12 time dependent nature of mechanically induced shear-layer turbulence to derive information
13 about strengths and limitations of the model. The validation procedure is tested for LES of
14 turbulent flow in a complex city, for which reference data from wind-tunnel experiments are
15 available. An initial comparison of mean flow statistics and frequency distributions was pre-
16 sented in part I. Part II focuses on comparing eddy statistics and flow structures. Analyses
17 of integral time scales and auto-spectral energy densities show that the tested LES repro-
18 duces the temporal characteristics of energy-dominant and flux-carrying eddies accurately.
19 Quadrant analysis of the vertical turbulent momentum flux reveals strong similarities be-

D. Hertwig
Meteorological Institute, University of Hamburg
Bundesstrasse 55, D-20146 Hamburg, Germany
Present address:
Department of Meteorology, University of Reading
P.O. Box 243, Reading, RG6 6BB, UK
E-mail: d.hertwig@reading.ac.uk
Tel.: +44-118-378-6721
Fax: +44-118-378-8905

G. Patnaik
Laboratories for Computational Physics and Fluid Dynamics
U.S. Naval Research Laboratory
Washington D.C., USA
E-mail: gopal.patnaik@nrl.navy.mil

B. Leitl
Meteorological Institute, University of Hamburg
Bundesstrasse 55, D-20146 Hamburg, Germany
E-mail: bernd.leitl@uni-hamburg.de

20 tween instantaneous ejection-sweep patterns in the LES and the laboratory flow, also show-
21 ing comparable occurrence statistics of rare but strong flux events. A further comparison
22 of wavelet-coefficient frequency distributions and associated high-order statistics reveals a
23 strong agreement of location-dependent intermittency patterns induced by resolved eddies
24 in the energy-production range.

25 The validation concept enables wide-ranging conclusions to be drawn about the skill of
26 turbulence-resolving simulations than the traditional approach of comparing only mean flow
27 and turbulence statistics. Based on the accuracy levels determined, it can be stated that the
28 tested LES is sufficiently accurate for its purpose of generating realistic urban wind fields
29 that can be used to drive simpler dispersion models.

30 **Keywords** Large-eddy simulation · Model validation · Quadrant analysis · Urban
31 environment · Wavelet analysis · Wind tunnel

32 1 Introduction

33 Time-dependent three-dimensional numerical simulations of turbulent flow originated from
34 meteorological research more than 40 years ago. Having its roots in the development of early
35 numerical weather prediction models [54,30], the first comprehensive applications of large-
36 eddy simulation (LES) in the context of turbulence research were made in the 1970s [14,
37 50]. With rapidly increasing computational capacities within the last decade or so LES and
38 other computational fluid dynamics (CFD) models became affordable for a broad research
39 community. This development is paralleled by the availability of commercial and open-
40 source codes and toolboxes.

41 Today, hardly any meteorological or wind engineering research area focusing on meso-
42 scale or micro-scale atmospheric processes is unaffected by the large eddy-resolving ap-
43 proach. LES is frequently applied to study problems in which the time-space evolution of the
44 atmospheric boundary-layer (ABL) is of special interest: e.g. stratification and diurnal trans-
45 formations of the ABL structure [35,29,4,12,3] or cloud physics [8,51]. Another key area
46 of application are flow and dispersion processes in the near-surface atmospheric boundary
47 layer over various surface forms ranging from homogeneous land types over mountainous
48 terrain [9,33] to plant or urban canopies [52,65,49,6,28].

49 It is increasingly recognised that studying transient (i.e. time-dependent) flow phenom-
50 ena is at least as important as the time-mean view of turbulence in order to characterise
51 ABL flows. While research on coherent flow structures initially had a strong focus on flow
52 over plant canopies [42,19], scientific interest is continuously shifting towards the connec-
53 tions between organised eddies and turbulent exchange in urban areas. Time-dependent,
54 three-dimensional numerical simulations like LES offer a space/time resolved view on ur-
55 ban turbulence and now play an important role in coherent structure research. The data, if
56 sufficiently quality controlled, can offer an ideal basis for fundamental research. Based on
57 data from direct numerical simulations, Coceal et al. [11], for example, presented a con-
58 ceptual model describing unsteady urban roughness-sublayer dynamics. Low momentum
59 streaks found above roof level were associated with the passage of hairpin vortices, an eddy
60 class composed of counter-rotating vortex structures that have been extensively studied in
61 flat-wall boundary-layer flows [43,2]. A second flow regime evolves in the shear layer on
62 top of the canopy. In this region, large-scale eddies are generated by the rolling-up of shear
63 zones and intermittent vortex shedding from rooftops. These structures travel downstream,
64 impinge on other buildings, and may interact with recirculation patterns in street canyons.

65 Within the urban canopy layer (UCL) Coceal et al. [11] found inclined vortex structures
66 with characteristic vorticity patterns that are of great importance for urban flow dynamics,
67 particularly regarding their influence on momentum, heat and pollutant transport.

68 1.1 Validation concept

69 The time-dependent nature of LES complicates the assessment of the quality of the predic-
70 tion and makes thorough validation of time-resolved simulations challenging. If conducted
71 at all, comparisons between LES and reference data, e.g. from experiments, are usually
72 restricted to mean flow and turbulence statistics. Strictly speaking, this only provides suffi-
73 cient insight about the accuracy of models based on the averaged conservation equations like
74 the Reynolds-averaged Navier-Stokes (RANS) equation models. In the case of turbulence-
75 resolving simulations such as LES, however, a thorough validation should also assess the
76 degree to which the code captures the transient structure of the flow. Established methods
77 from the field of signal analysis and flow pattern recognition can open up new ways to define
78 quality criteria by which to assess the model output.

79 In part I we introduced a holistic LES validation concept for near-surface atmospheric
80 flow based on a sequence of well-established time-series analysis methods. The essential
81 premise here is that the time-dependent nature of LES has to be taken into account for the
82 validation to provide a true assessment of the capabilities and limitations of the model. The
83 proposed validation hierarchy distinguishes three comparison levels:

- 84 1. Exploratory data analysis (*here: descriptive statistics, frequency distributions*)
- 85 2. Analysis of turbulence scales (*here: temporal autocorrelations, energy density spectra*)
- 86 3. Flow structure identification (*here: quadrant analysis, continuous wavelet transform*).

87 The three levels offer increasingly deeper insight into the simulation properties in terms
88 of the representation of turbulence structures, but also make increasingly higher demands
89 on the quality and quantity of reference data.

90 1.2 Test scenario, data and study layout

91 We test the validation approach based on a particularly challenging scenario: turbulent flow
92 in a densely built-up urban centre. A detailed account of relevant information about the test
93 scenario, the LES and the laboratory experiment was presented in part I. For the sake of
94 brevity, we only provide an overview here.

95 The high-density city centre of Hamburg, Germany, serves as the test bed for the vali-
96 dation exercise. The inner city is characterised by an average building height of $H = 34.3$ m
97 with typical street canyon widths in the order of $W = 20$ m. This results in a typical street-
98 canyon aspect ratio in the inner city of $H/W = 1.72$. The LES tested is the urban aero-
99 dynamics code FAST3D-CT [40, 39], developed and operated by the U.S. Naval Research
100 Laboratory. The code uses an implicit representation of subgrid-scale turbulence, which is a
101 very efficient approach for LES in large urban domains with high spatial resolution. In this
102 study the simulation was run with a spatial resolution of 2.5 m within the urban roughness
103 sublayer in a $4 \text{ km} \times 4 \text{ km}$ computational domain. The purpose of this particular simulation
104 was the provision of realistic urban wind data that can be used off-line to drive an urban
105 plume dispersion model.

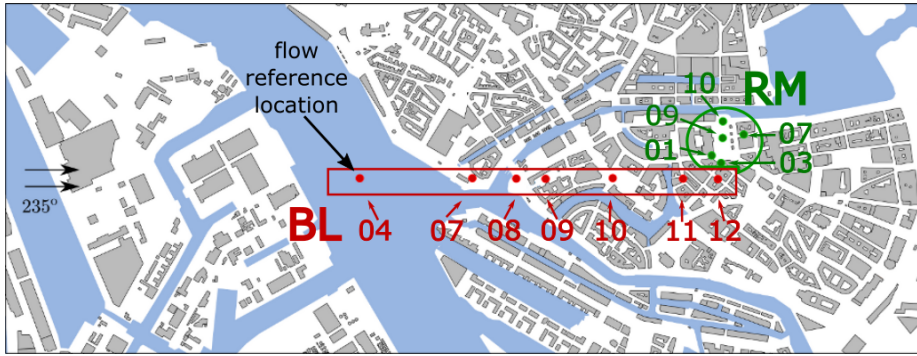


Fig. 1: Wind-tunnel model area indicating the boundary-layer development positions (prefix *BL*, red dots) and selected sites around the city hall (prefix *RM*, green dots). The Elbe river separates the high-density city centre to the north from the low-rise industrial harbour region. The flow reference location above the river (BL04) is also indicated.

106 Point-wise velocity time series were extracted at cell centres every 0.5 s over a duration
 107 of 23,250 s (approx. 6.5 h). Time-resolved, point-wise reference data have been generated
 108 using laser Doppler anemometry (LDA) in a boundary-layer wind tunnel based on a detailed
 109 scale representation of the urban test area (geometric scale: 1:350). The longitudinal/lateral
 110 extents of the wind-tunnel model were 3.7 km/1.4 km full-scale (10.5 m/4 m in model scale).
 111 The model area is shown in Fig. 1 together with the locations of the comparison sites that
 112 is focused on in the following sections (for a detailed discussion of local geometry and flow
 113 pattern at these sites see part I). With the LDA system, two velocity components (U - V or
 114 U - W pairs) were simultaneously measured over a duration of 170 s (16.5 h under full-scale
 115 conditions). When operated in U - W mode, the LDA measuring volume and the probe itself
 116 are aligned at the same height. In order to avoid physical interferences with model buildings,
 117 measurements of the vertical velocity component were only conducted at locations above the
 118 UCL ($z \geq 1.2H$) at the BL sites. For time series analyses the discontinuous LDA signals
 119 were reconstructed using a sample-and-hold technique.

120 In the first part of the study we covered the initial level of the validation concept by
 121 comparing mean flow and turbulence statistics. This was extended by the analysis of the
 122 underlying velocity time series in terms of frequency distributions, which documented the
 123 strength of the tested code to capture characteristic urban flow features.

124 In the following, we focus on the comparative analysis of turbulence scales and trans-
 125 sient flow patterns in the urban roughness sublayer. The analysis methods used in this study
 126 are introduced in Sect. 2. We then follow the second and third levels of the validation strat-
 127 egy by comparing temporal auto-correlations, turbulence integral time scales and spectral
 128 energy densities (Sect. 3) and apply flow pattern recognition techniques (conditional resam-
 129 pling and joint time frequency analyses) in Sect. 4. The fitness of the proposed methodology
 130 for a detailed LES validation is discussed in Sect. 5 along with final conclusions and recom-
 131 mendations for next steps.

132 2 Analysis methods

133 In the following we present an overview of the methods applied to analyse and compare
 134 eddy statistics and flow patterns based on single-point time-resolved velocity signals. A
 135 fixed Cartesian model coordinate system (x, y, z) is used and the corresponding streamwise
 136 (longitudinal), spanwise (lateral) and vertical components U_i ($i = 1, 2, 3$) of the velocity vec-
 137 tor are denoted as U, V and W . Overbars denote time-averaged quantities. Velocity statistics
 138 are non-dimensionalised based on the mean streamwise reference velocity U_{ref} at a refer-
 139 ence height of $z_{ref} = 45.5$ m ($1.33H$) above ground upstream of the inner city area (Fig.
 140 1).

141 2.1 Integral time scales and energy spectra

142 Turbulence integral time scales can be determined from velocity fluctuation time series
 143 based on temporal autocorrelations. For stationary flow the 1D autocorrelation function of
 144 the fluctuating i th velocity component, $u'_i = U_i - \bar{U}_i$, with $u'_1 = u', u'_2 = v', u'_3 = w'$, as a
 145 function of time lag t_l is given by

$$R_{ii}(t_l) = \frac{1}{\sigma_i^2} \overline{(U_i(t) - \bar{U}_i(t)) (U_i(t + t_l) - \bar{U}_i(t + t_l))}. \quad (1)$$

146 R_{ii} describes the degree of common variation in a variable depending on the time dif-
 147 ference between two observations, and hence is a measure of the flow memory [55,31].
 148 Motions separated by sufficiently long lags become statistically independent and $R_{ii} \rightarrow 0$
 149 [57]. The integral time scale τ_{ii} is obtained from

$$\tau_{ii} = \int_{t_0}^{t_{\infty}} R_{ii}(t_l) dt_l. \quad (2)$$

150 Different specifications of the upper integration limit t_{∞} can be used, e.g. as the zero-
 151 crossing point of R_{ii} or as the time after which R_{ii} has dropped below a critical value [38].
 152 The computations can become ambiguous in cases where R_{ii} does not decrease monoton-
 153 ically, but instead oscillates or does not drop to zero within the maximum recorded time
 154 interval. The physical relevance of such oscillations is debatable [64]. In this study it is as-
 155 sumed that they reflect the increasingly uncertain nature of R_{ii} at large time lags (i.e. smaller
 156 sample sizes). This is supported by the fact that the intensity of the tail oscillations is related
 157 to the overall duration of the signal and hence to the statistical representativeness obtained
 158 from the respective averaging times. In order to consistently derive τ_{ii} we use an extrapo-
 159 lation approach for the tails [20]. While the bulk of the original R_{ii} function is preserved at
 160 small time lags, the curvature of its tail is approximated by an exponential decay (Fig. 2).
 161 The upper integration limit t_{∞} is then defined as the time after which $R_{ii}^{fit} \leq 0.01$.

162 Spectral energy-density functions $E_{ii}(f)$ provide information about the distribution of
 163 the signal's variance among different eddy scales. Due to the component resolution of the
 164 experimental data available in this study, the analysis concentrates on the comparison of 1D
 165 spectra and co-spectra of two velocity components. Fourier coefficients $\hat{u}_i(f)$ of velocity
 166 fluctuations $u'_i(t)$ are derived from a fast Fourier transform (FFT) based on the Cooley-
 167 Tukey algorithm [13]. Taking the example of the streamwise fluctuations, the one-sided
 168 auto-spectral energy densities are obtained according to

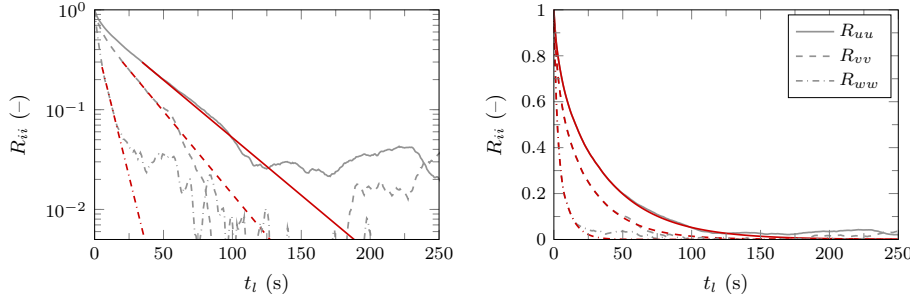


Fig. 2: Example of the fitting procedure applied to the R_{ii} functions (here: wind tunnel data). Left: original curves together with the respective tail fit; right: concatenated signals using the original and fitted curves. The original curves are retained up to time lags for which R_{ii} has dropped to a value between once or twice its e -folding time.

$$E_{uu}(f_k) = \frac{2}{Nf_s} \widehat{u}_k^* \widehat{u}_k = \frac{2}{N^2 \delta f_s} |\widehat{u}_k|^2, \quad (3)$$

169 with the frequency index $k = 0, \dots, N/2$, N is the number of samples in the signal,
 170 f_s is the sampling frequency, $\delta f_s = f_k - f_{k-1}$ is the constant frequency increment and the
 171 asterisk denotes the complex conjugate [36]. In the same way energy density spectra E_{vv}
 172 and E_{ww} can be derived from spanwise and vertical velocity fluctuations, v' and w' . For
 173 paired signals of u' and w' the co-spectrum Co_{uw} is computed according to $\text{Co}_{uw}(f_k) =$
 174 $\text{Re}\{\widehat{u}_k\} \text{Re}\{\widehat{w}_k\} + \text{Im}\{\widehat{u}_k\} \text{Im}\{\widehat{w}_k\}$.

175 Earlier studies have shown that the unique roughness structure of urban surfaces leaves
 176 a distinct footprint in the spectra [45, 46]. Inertial subrange behaviour in urban areas in terms
 177 of $-5/3$ slopes is comparable to flow over uniform roughness. However, based on a more
 178 stringent test for local isotropy, Rotach [45] found that urban flow is not truly isotropic in the
 179 inertial subrange at heights well within the roughness sublayer. The size of integral length
 180 scale eddies associated with the spectral peaks deviates from empirical reference relations
 181 for flow over homogeneous surfaces [25]. Roth [46] reported that within the UCL and in
 182 the vicinity of the canopy top, a shift towards higher frequencies is evident in the spectra
 183 of the horizontal velocities, while peaks in vertical velocity spectra are offset towards lower
 184 frequencies. The increase of the vertical eddy-length scale suggests that the vertical transport
 185 is dominated by wake turbulence that scales with the building dimensions.

186 2.2 Conditional averaging

187 A well-known representative of conditional resampling/averaging methods is the quadrant
 188 analysis [60, 61, 59], which can be applied, for example, to analyse the vertical turbulent
 189 momentum exchange $\overline{u'w'}$. Instantaneous fluxes $u'w'$ are grouped into one of four quadrants
 190 based on the respective composition of the algebraic signs of u' and w' . Following the nota-
 191 tion by Raupach [41], conditional averages of the momentum flux contributions from each
 192 of the four quadrants are obtained from

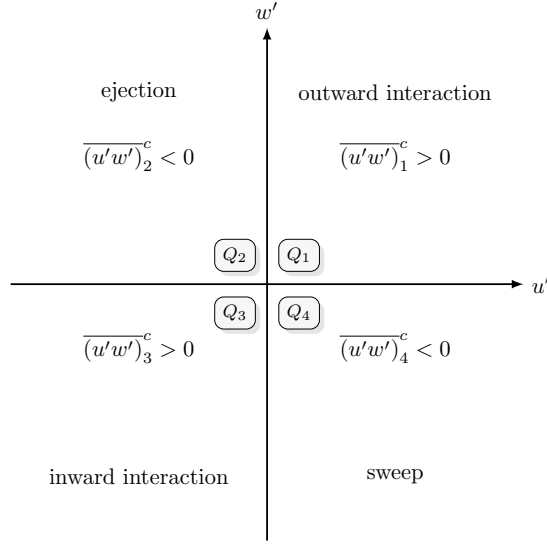


Fig. 3: The four quadrants of the vertical turbulent momentum flux $u'w'$.

$$\overline{(u'w')}_i^c = \lim_{T \rightarrow \infty} \frac{1}{T} \int_0^T u'(t)w'(t)I_i(t)dt, \quad (4)$$

193 where c is a reminder for the conditional nature of the time-average, T is the signal
 194 duration, and $I_i(t)$ is a trigger function yielding 1 if $u'(t)$ and $w'(t)$ are in the i th quadrant
 195 and 0 otherwise. The relative contributions from individual quadrants to the total flux $\overline{u'w'}$
 196 are measured in terms of flux fractions $S_i = \overline{(u'w')}_i^c / \overline{u'w'}$, where $\sum_i S_i = 1$.

197 Fig.3 shows a schematic of the quadrant separation of the instantaneous momentum flux
 198 $u'w'$. In the first and third quadrant, Q_1 and Q_3 , u' and w' are of the same sign and conditional
 199 averaging results in positive fluxes $\overline{(u'w')}_{1,3}^c > 0$. Corresponding fluid motions are denoted
 200 as outward and inward interactions [60]. The second quadrant, Q_2 , is associated with the
 201 upward ejection of momentum ($u' < 0, w' > 0$). The opposing process is the downward
 202 sweep of momentum ($u' > 0, w' < 0$; Q_4). Conditionally averaging over ejection and sweep
 203 events results in negative fluxes $\overline{(u'w')}_{2,4}^c < 0$. The difference $\delta S_{4,2} = S_4 - S_2$ quantifies
 204 the local dominance of ejection or sweep contributions. The flux exuberance $Ex = (S_1 +$
 205 $S_3)/(S_2 + S_4)$ is a measure of the relative importance of organised gradient motions ($Q_{2,4}$)
 206 over counter-flux events ($Q_{1,3}$) for the local flux balance [53, 10].

207 The instantaneous fluxes $u'w'$ can by far exceed the magnitude of $\overline{u'w'}$. To determine the
 208 relative importance of large amplitude contributions to the flux fractions, Willmarth and Lu
 209 [61] proposed to analyse fluctuation combinations that exceeds a specified threshold. This
 210 approach is known as hole-size analysis and allows the comparison of occurrence probabili-
 211 ties of extreme flux events in LES and experiment. Following Raupach [41], the successive
 212 filtering of extreme events is implemented by adding another constraint on the trigger func-
 213 tion I_i by only averaging over fluxes for which $|(u'w')_i| \geq H_c |\overline{u'w'}|$, with H_c being the hole
 214 size ($H_c = 0, 1, 2, \dots, 30$ in this study).

215 Within and above the UCL building-induced turbulence can induce strong turbulent mix-
 216 ing [46]. Through the analysis of the vertical momentum flux, the relative contributions of
 217 the upward transport of momentum deficit (ejection) and the downward transport of mo-
 218 mentum excess (sweep) in urban environments can be investigated [44]. At roof-level, the
 219 momentum exchange is often found to be dominated by sweeps. However, this prevalence
 220 vanishes at higher elevations. The dominance of sweeps within the UCL has been confirmed
 221 on the basis of field observations [37, 10], showing that ejections are prevailing well above
 222 the canopy. Oikawa and Meng [37] described characteristic sweep and ejection patterns as-
 223 sociated with sudden fluid bursts and connected distinctive ramp structures in temperature
 224 signals with the passage of large-scale coherent eddies above the canopy. Based on condi-
 225 tional averages of ejection-sweep cycles within and above a street canyon, Feigenwinter and
 226 Vogt [18] showed that fluctuation levels were highest just above the canopy and decreased
 227 with increasing distance from the roofs. Christen et al. [10] described the role of coherent
 228 structures for turbulent exchange at the interface between canopy and roughness sublayer by
 229 associating ejection-sweep events with the advection and penetration of coherent structures
 230 from the roughness layer into the street canyon.

231 2.3 Joint time-frequency analysis

232 The wavelet transform is an important representative of joint time-frequency analysis meth-
 233 ods used for the time-localisation of a signal's frequency content [34, 22, 23]. In effect, this
 234 approach adds the time dimension to the classic Fourier analysis by using wave functions of
 235 limited temporal support instead of non-local sinusoids. In the application to turbulent flows
 236 this means that the occurrence of eddy structures associated with certain frequencies can be
 237 studied in a time-dependent framework [32, 15].

238 Wavelets are oscillating, square-integrable, localised functions whose location and shape
 239 are manipulated during the transform process to unfold the time-frequency content of the
 240 signal [1]. The wavelet function $\psi_{s,n}(t) = s^{-1/2}\psi[(t-n)s^{-1}]$ depends on two parameters.
 241 The translation parameter n shifts the wavelet along the time axis and the dilation parameter
 242 $s > 0$, also known as the scale of the wavelet, stretches ($s > 1$) or compresses ($0 < s < 1$)
 243 the function in order to retrieve low or high frequency information from the signal. This
 244 behaviour is illustrated in Fig. 4. The normalisation factor $s^{-1/2}$ ensures finite energy content
 245 at all wavelet scales [26]. The continuous wavelet transform (CWT) of a time-dependent
 246 signal $\Phi(t)$ with zero mean and finite energy is given by

$$W_n(s) = \frac{1}{\sqrt{s}} \int_{-\infty}^{\infty} \Phi(t) \psi^* \left(\frac{t-n}{s} \right) dt, \quad (5)$$

247 where the asterisk denotes the complex conjugate. The wavelet coefficients $W_n(s)$ con-
 248 tain time-frequency information about $\Phi(t)$. The time-frequency resolution of the CWT is
 249 variable. At large scales, the wavelet is less well localised in time than at small scales, while
 250 the frequency resolution is better than for contracted wavelets (Fig. 4). Like the Fourier
 251 transform, the CWT is reversible and the original signal can be reconstructed from the
 252 wavelet coefficients without information loss [36].

253 For our analyses of velocity time series we use the complex Morlet wavelet defined as
 254 $\psi_m(t) = N_{\psi_m} \exp(i\omega_0 t) \exp(-t^2/2)$. The central frequency ω_0 is set to a value of 6 in this
 255 study, and $N_{\psi_m} = \pi^{-1/4}$ is a normalisation factor. We apply a discretised version of the CWT
 256 in spectral space [1, 56]. For a discrete signal $\Phi_n = \Phi(t_n = n \delta t_s)$ sampled at time intervals

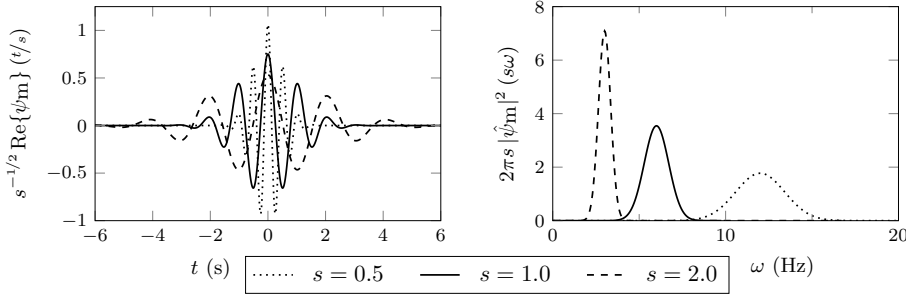


Fig. 4: Influence of the dilation parameter s on the shape of the Morlet wavelet in the time (left) and frequency domain (right), with the latter showing the wavelet's energy spectrum.

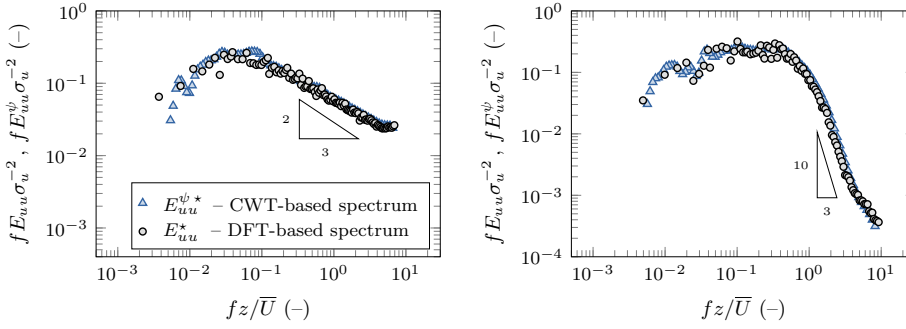


Fig. 5: Scaled auto-spectral energy densities of the streamwise velocity derived from the discrete-time CWT using the Morlet wavelet (triangles) in comparison to the classic discrete Fourier transform (DFT) spectra (dots). Left: wind tunnel; right: LES. The spectra correspond to a height of 45.5 m above the Elbe river (site BL04).

257 δt_s over a duration of $T = N\delta t_s$, where N is the number of samples and $n = 0, \dots, N-1$, the
 258 discrete-time CWT is given by

$$W_n(s) = \sqrt{\frac{2\pi s}{\delta t_s}} \sum_{k=0}^{N-1} \hat{\Phi}_k \hat{\psi}^*(s\omega_k) \exp(i\omega_k n \delta t_s), \quad (6)$$

259 where $\hat{\Phi}$ and $\hat{\psi}$ are the Fourier transforms of the signal and the wavelet, respectively, k
 260 is a frequency index and $\omega = 2\pi f$. The term before the sum is a normalisation factor that
 261 ensures that the wavelet function has unit energy at each scale. The Fourier transform of the
 262 Morlet wavelet is known analytically: $\hat{\psi}_m(\omega) = N_{\psi_m} \mathcal{H}(\omega) \exp(-(\omega - \omega_0)^2/2)$, where \mathcal{H}
 263 is the Heaviside step function [56]. Eq. (6) is implemented by obtaining the inverse Fourier
 264 transform of the product of $\hat{\Phi}_k$ and $\hat{\psi}^*(s\omega_k)$ for all scales s at all translations n using an
 265 FFT algorithm [13]. Following [56], the series of scales s_j is obtained as a fractional power
 266 of 2 according to $s_j = s_0 2^{j\delta j}$, where s_0 is the smallest scale and δj is the spacing between
 267 scales. In this study we use $s_0 = \delta t_s$ and $\delta j = 1/8$ following sensitivity tests.

268 As the energy content of the signal is conserved in wavelet space, it is possible to obtain
 269 a global energy density spectrum based on $W_n(s)$ similar to the spectrum available from the

270 discrete Fourier transform [1]. Fig. 5 shows wind tunnel and LES energy-density spectra
 271 corresponding to a height of 45.5 m above the Elbe river derived from a discrete-time CWT
 272 using the complex Morlet wavelet in comparison to the classic Fourier spectra. Both, the
 273 $-2/3$ slope of the wind-tunnel inertial subrange as well as the much steeper slope of the LES
 274 spectrum (approximately $-10/3$ as a result of cutting off eddies smaller than the numerical
 275 grid) are very well resolved with the CWT. This fast energy decay is characteristic for LES
 276 spectra due to the spatial filtering and can only be adequately resolved with wavelets that
 277 have a high number of vanishing moments. With the Morlet wavelet using $\omega_0 = 6$ spectral
 278 slopes up to -7 can be reproduced [16].

279 3 Eddy statistics

280 In the following sections we present results of the validation test case based on detailed
 281 analyses of velocity time series. Results are only directly compared at heights for which the
 282 largest spatial offset between the LES and wind-tunnel data pairs was 0.25 m. This offset is
 283 well within the LDA's spatial accuracy of 0.56 m full scale in z -direction when operated in
 284 U - V mode or in y -direction for U - W measurements (see part I for details).

285 The validation results presented in the following paragraphs and in Sect. 4 represent
 286 only a subset of the analyses performed in the course of the validation study in order to
 287 focus on particular strengths and limitations of the model. The selection is representative of
 288 the overall agreement between experiment and LES.

289 3.1 Integral time scales

290 Integral time scales can be regarded as representative time scales of the dominant turbulence
 291 structures in the flow. Comparing their characteristics is therefore particularly important for
 292 eddy-resolving approaches such as LES.

293 In the following, comparisons of τ_{ii} and R_{ii} are presented in full-scale dimensions. The
 294 full-scale time lags t_l used to construct $R_{ii}(t_l)$ were derived from their dimensionless equiv-
 295 alents t_l^* according to $t_l^* = t_l U_{ref} L_{ref}^{-1}$, setting U_{ref} to 5 m s^{-1} and using reference lengths,
 296 L_{ref} , of 1 m for the laboratory flow and an equivalent of 350 m for the LES.

297 3.1.1 Vertical structure of τ_{ii}

298 Fig. 6 shows height profiles of Eulerian integral time scales for the three velocity compo-
 299 nents within the roughness sublayer up to approximately $2H$ at four of the BL comparison
 300 sites, for which measurements of all three velocity component are available from the refer-
 301 ence experiment. The statistical reproducibility of the experimental results was derived from
 302 repetition measurements, yielding full-scale maximum scatter of $\tau_{11} \pm 3.95 \text{ s}$, $\tau_{22} \pm 1.85 \text{ s}$,
 303 and $\tau_{33} \pm 1.17 \text{ s}$.

304 Overall, the LES captures the qualitative height-dependence of the integral time scales
 305 at most of the sites. While there are some quantitative differences, the overall magnitude of
 306 turbulence time scales agrees with the experiment. A steady increase of τ_{ii} is seen well above
 307 roof level, corresponding to an increase of eddy length scales in response to the gradual
 308 weakening of topology-induced flow effects. However, at site BL07 the decrease of the LES
 309 τ_{11} and low values of τ_{33} above H is opposite to the behaviour seen in the experiments.
 310 This site is located in the region where an internal boundary layer is starting to develop just

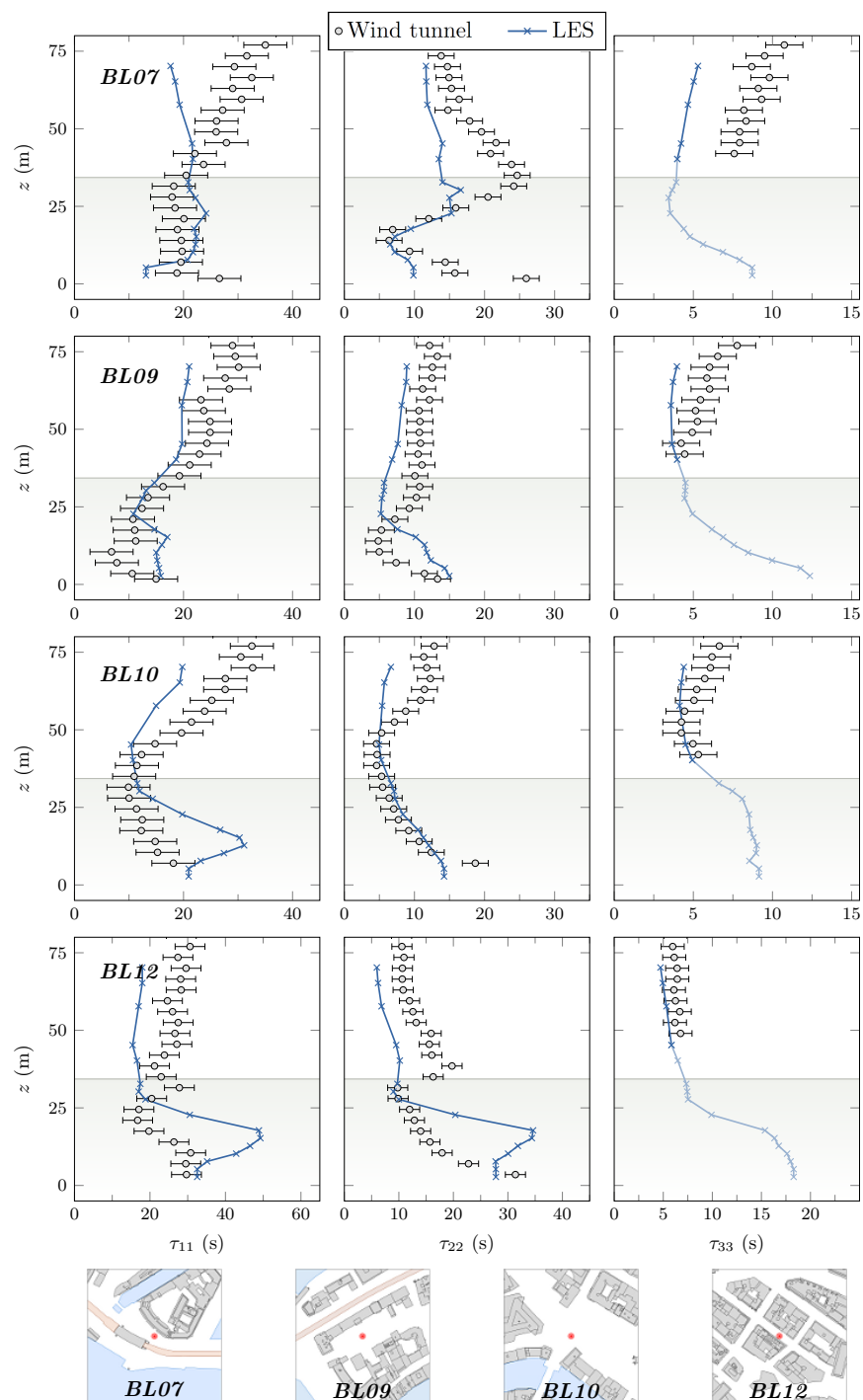


Fig. 6: Comparison of height profiles of τ_{11} (left column), τ_{22} (centre) and τ_{33} (right) at four comparison locations (wind tunnel: dots; LES: crosses). The grey shading indicates heights lower than the mean building height of $H = 34.3$ m in the city centre. Maps showing the location of the comparison points depict an area of $210 \text{ m} \times 210 \text{ m}$. Times are given in full scale.

311 downstream of the river in response to the increased surface roughness of the high-density
 312 inner city. Here it seems that the upper layer flow field in the LES still is dominated by the
 313 artificial turbulence prescribed at the inflow plane of the simulation. Further downstream, as
 314 the flow adjusts to the new roughness underneath, the simulation above the UCL becomes
 315 more self-consistent, resulting in an increased level of agreement with the wind tunnel.

316 The same is true for the height development of integral time scales τ_{33} associated with
 317 the vertical velocity from site BL07 to BL12. At elevations at which measurements are
 318 available, the τ_{33} of the LES are well within the experimental scatter at most heights in the
 319 downtown area (BL09–BL12). Within the UCL the LES predicts increased amplitudes of τ_{33}
 320 (BL09, BL12), indicating enhanced memory effects associated with the vertical momentum
 321 exchange, for example associated with street-canyon ventilation at site BL12. Although di-
 322 rect validation of this simulation feature is not possible here due to the lack of experimental
 323 data points, the agreement of the magnitudes of τ_{11} and τ_{22} indicates that this is also true for
 324 τ_{33} for consistency reasons.

325 The overall height structure of τ_{ii} uniquely corresponds to the local building topology
 326 and thus changes strongly from site to site. For example, at sites BL10 (intersection) and
 327 BL12 (street canyon) strong vertical gradients in τ_{11} and τ_{22} can be observed within the
 328 UCL; a feature that is more pronounced in the LES. At all sites the wind-tunnel flow is
 329 characterised by long τ_{22} well within the UCL, indicating the existence of comparatively
 330 long-lived eddy structures. These features are also evident in the LES, although the peak
 331 heights and magnitudes differ at some of the locations, e.g. BL12.

332 By comparing integral time scales at various sites, it could be shown that the LES re-
 333 sponds in a similar way to the local building morphology as the flow in the reference experi-
 334 ment. Here it is particularly important to analyse all three components of the velocity vector,
 335 as the urban flow field is highly three-dimensional and the LES should be able to reflect this
 336 complexity. This is crucial, for example, for the representation of horizontal and vertical
 337 mixing in turbulent dispersion processes. The results demonstrate the ability of the tested
 338 LES code to represent the time-scales of energy-dominating turbulence features realistically
 339 for the given application, even in a very complex geometry and with limitations imposed by
 340 the grid resolution.

341 3.1.2 Structural information from R_{ii}

342 It is worthwhile to also investigate the shapes of the underlying temporal autocorrelation
 343 curves, $R_{ii}(t_l)$ in order to derive further information about eddy structures.

344 Two commonly observed features are shown in Fig. 7, depicting close-ups of LES and
 345 wind tunnel data at short time lags. Strikingly different curvatures of the LES and laboratory
 346 autocorrelations can be observed at $t_l \leq 10$ s. While the experimental curves are more-
 347 or-less straight lines, indicating a fast exponential decay (note the use of logarithmic y-
 348 axes), the eddies in the LES are slightly longer correlated over short times. This feature is
 349 characteristic of the spatially filtered nature of the LES, in which only the large eddies are
 350 directly resolved. As discussed by Townsend [57], in turbulent flows in which eddy sizes are
 351 in some way restricted the slope of the R_{ii} functions is rather gentle at short time lags. If, on
 352 the other hand, a wide and continuous range of eddy structures is present in the flow, as is
 353 the case in the wind tunnel, the initial slope is significantly steeper.

354 Another noticeable feature encountered at various locations in the urban domain is that
 355 some of the autocorrelation functions are composed of rapidly and slowly varying parts,
 356 a feature that is often more pronounced in the autocorrelations of the streamwise velocity
 357 fluctuations. The example of location RM10 (Fig. 7, left) shows that in both data sets the

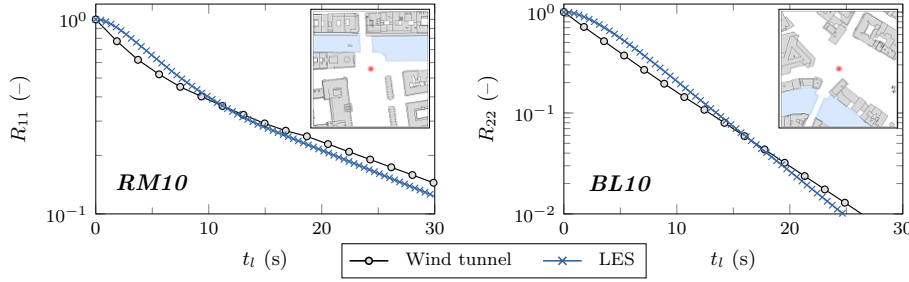


Fig. 7: Autocorrelation functions at two example locations in the inner city for the wind tunnel (dots) and the LES (crosses). Left: R_{11} at location RM10 in a height of 40.25 m ($1.2H$); right: R_{22} at location BL10 in a height of 28 m ($0.8H$). Time lags are presented in full scale.

358 R_{11} slopes are clearly steeper for time lags below 10 s, approximately corresponding to the
 359 e -folding time of the functions, than for the remaining time periods. This is an indication
 360 of the superposition of two autocorrelation functions and associated dominant eddy time
 361 scales (e.g. discussions in [57,31]). Due to the complexity of urban flow fields, at certain
 362 positions the flow may locally be dominated by more than one regime of turbulent motions
 363 with different length and time scales of associated eddy classes.

364 3.2 Energy density spectra

365 Energy density spectra are utilised to comparatively evaluate the distribution of energy
 366 among eddies present in the flow and to compare frequency bandwidths corresponding to
 367 spectral energy peaks, which have a direct relation to τ_{ii} . From LES it is expected that
 368 energy-containing turbulence is directly resolved, ideally well into the inertial subrange.
 369 Formally, the effective resolution of the LES is coupled to the grid size, which acts as a spa-
 370 tial filter, and to the properties of the employed numerical methods. In addition, the nature of
 371 the flow has an influence on local resolution characteristics. The overall length scales of the
 372 energy-dominating eddies within the UCL, for example, are smaller than those encountered
 373 in the inertial sublayer. In the LES code evaluated here only structures sufficiently larger
 374 than 2.5 m are directly resolved. Hence it needs to be evaluated whether this grid resolution
 375 is sufficient to resolve even the comparatively small-scale energy-dominating eddy ranges
 376 associated with typical canopy-layer turbulence.

377 Fig. 8 (first three rows) shows examples of the local agreement between wind tunnel and
 378 LES auto-spectra above the mean building height ($1.3H$). As is apparent from these plots,
 379 in the densely built-up city centre the mean LDA sampling rates achieved in the wind tunnel
 380 were too low to fully resolve the inertial subrange portion of the flow. Due to enhanced mix-
 381 ing in the urban roughness sublayer the LDA particle seeding is more homogeneous, but less
 382 dense on average than in the approach flow. Nevertheless, at all locations the time-resolution
 383 of the experimental data is sufficient to directly compare with the energy-containing spectral
 384 ranges resolved by the LES.

385 For all velocity components and all comparison points the agreement between the LES
 386 and wind-tunnel spectra is remarkably good in the low-frequency range that is associated
 387 with large, anisotropic eddies. The spectral peak regions agree well over the range of mor-

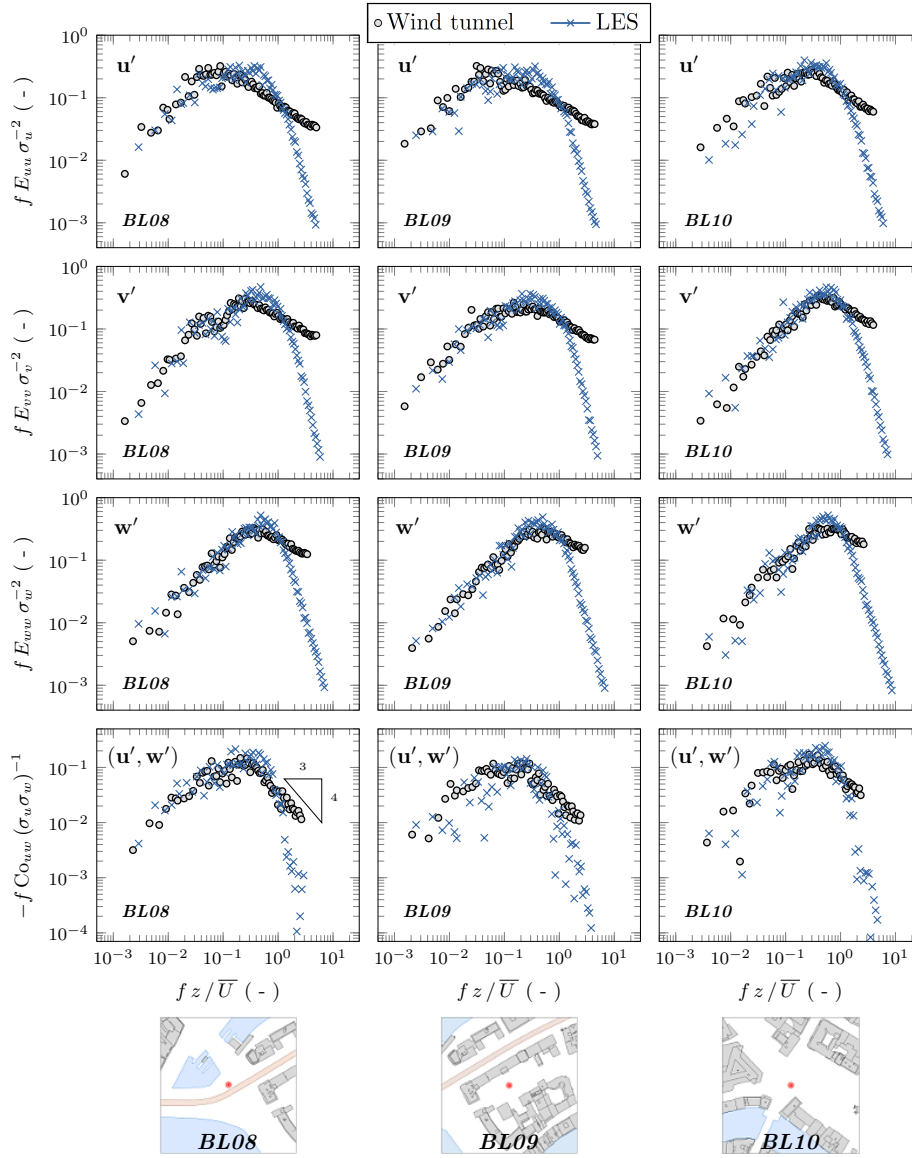


Fig. 8: Comparison of wind tunnel (dots) and LES (crosses) auto-spectral energy densities and co-spectra (bottom row) at three different locations in a height of $1.3H$ (45.5 m). The respective velocity component analysed, i.e. u' , v' , w' or (u', w') , is indicated in the plots. The spectra are presented in a referenced framework based on the mean streamwise velocity \bar{U} and the velocity variance σ_i^2 at height z . Maps show the location of the comparison sites and their immediate surroundings.

388 phologically rather different comparison sites. The fast roll-off of the numerical spectra at
 389 high frequencies is quite apparent, starting approximately after one decade into the inertial
 390 subrange. An interesting double-peak pattern in the v' -spectra is evident at site BL08 in
 391 both the laboratory and the simulation, implying a structural change in the flow. While the
 392 first peak corresponds to the peak frequency range characteristic for the approach flow (see
 393 BL04 spectra shown in Fig. 5), the second peak agrees well with the frequencies determined
 394 further downstream at the city locations (e.g. BL09, BL10). The increasing influence of the
 395 urban roughness on the flow field above the canopy is reflected in the fact that the size of
 396 the energy-containing eddies, measured by the frequency location of the energy peaks, is
 397 gradually decreasing. A similarly good agreement between both data sets is also seen below
 398 roof level at $0.5H$ (not shown).

399 The bottom row of Fig. 8 shows co-spectra, Co_{uw} , of the streamwise and vertical velocity
 400 fluctuations. Compared to the auto-spectra the inertial-subrange slopes of the co-spectra are
 401 much steeper with a $-4/3$ power-law decay [63,25]. This indicates the importance of large
 402 eddies for the vertical turbulent momentum exchange $\overline{u'w'}$ in the urban roughness sublayer.
 403 At all sites, the roll-off of the LES spectra is considerably faster, in agreement with the
 404 findings for the auto-spectra. Overall the flux-dominating frequency ranges in the LES agree
 405 very well with the wind tunnel. Even complex features like the double-peak pattern observed
 406 at location BL10 are remarkably well captured. In both data sets, the spectral maxima are
 407 shifting towards higher frequencies from the river site BL04 (not shown) to the downstream
 408 street canyon sites. This shows that the LES captures the increasing influence of the urban
 409 environment on the flow and the importance of building-induced turbulence for vertical
 410 turbulent mixing.

411 4 Flow structures

412 The previous analyses are classic ways to infer information about the structure of turbulence,
 413 characteristic scales of dominant eddies and associated contributions to the variance of the
 414 flow field. In the next and final level of the validation study we now extend this analysis
 415 by investigating the dynamics of eddy structures by means of conditional resampling of the
 416 vertical momentum flux and joint time-frequency analysis.

417 4.1 Quadrant analysis

418 The comparison of the (u', w') co-spectra showed that the LES provides a realistic picture
 419 of the average flux contributions from different eddy classes. In the following, the structure
 420 of the instantaneous vertical turbulent momentum flux $\overline{u'w'}$ is examined with quadrant anal-
 421 ysis. In a first step, the flux fractions defined in Eq. (4) are related to the associated joint
 422 probability density function (JPDF) of u'/U_{ref} and w'/U_{ref} . This approach provides a 2D
 423 extension of the analysis of velocity frequency distributions presented in part I.

424 Fig. 9 shows comparisons of JPDFs at two example locations in a height of $z = 1.3H$:
 425 site BL07, located just downstream of the river upstream of the city core, and the downtown
 426 site BL10 at a complex intersection. Qualitatively, the overall shapes and extents of the
 427 joint PDFs in the $(u'/U_{ref}, w'/U_{ref})$ plane agree well. At both locations, the semi-major
 428 axes of the ellipses proceed through the Q_2 and Q_4 quadrants, indicating that the largest
 429 instantaneous flux amplitudes are associated with ejection and sweep episodes. At site BL07
 430 both joint PDFs are fairly symmetrical about the semi-major and semi-minor axes, with

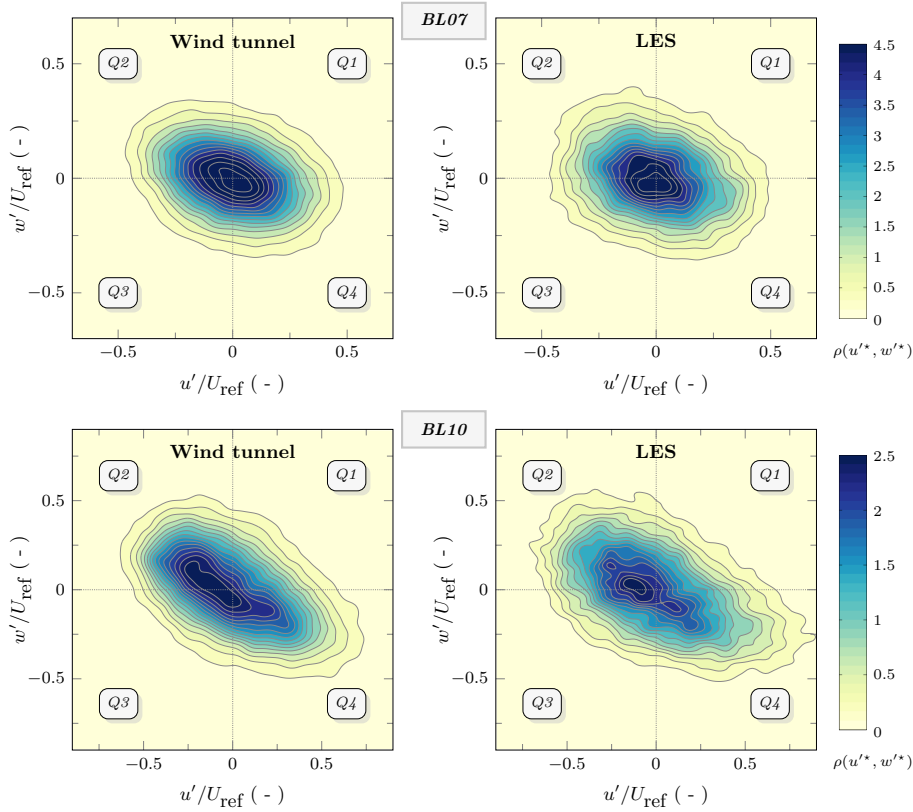


Fig. 9: Joint probability density functions of the streamwise and vertical velocity fluctuations in the wind tunnel (left) and the LES (right) for two comparison sites at $z = 1.3H$ (45.5 m). Note that $u^* = u'/U_{ref}$ and $w^* = w'/U_{ref}$ in the legend. See insets in Fig. 10 for the locations of sites BL07 and BL10.

431 the peaks being centred at low amplitudes of u'/U_{ref} and w'/U_{ref} . This picture changes
 432 significantly when investigating the flow above the city centre, which is increasingly affected
 433 by the change in the underlying surface roughness. At BL10 the LES and the wind tunnel
 434 both show an overall increase of high-amplitude fluxes in the Q_2 and Q_4 quadrants. However,
 435 while the distribution peaks both shift away from the centre into the low-amplitude region
 436 of the ejection quadrant (Q_2), strong downward motions (sweeps, Q_4) at this location are
 437 occurring more often than their ejection counterparts. The larger variability observed in
 438 the LES probability contour lines is associated both with the eddy-scale truncation in the
 439 simulation and with the shorter duration of the LES signals compared to the experiment.

440 4.1.1 Flux fraction profiles

441 Vertical profiles of flux fractions S_i , local sweep-ejection differences $\delta S_{4,2}$ and of the exu-
 442 berance parameter Ex above the UCL are shown in Fig. 10 at three sites. Since ejection and
 443 sweep episodes are associated with coherent turbulence structures primarily associated with

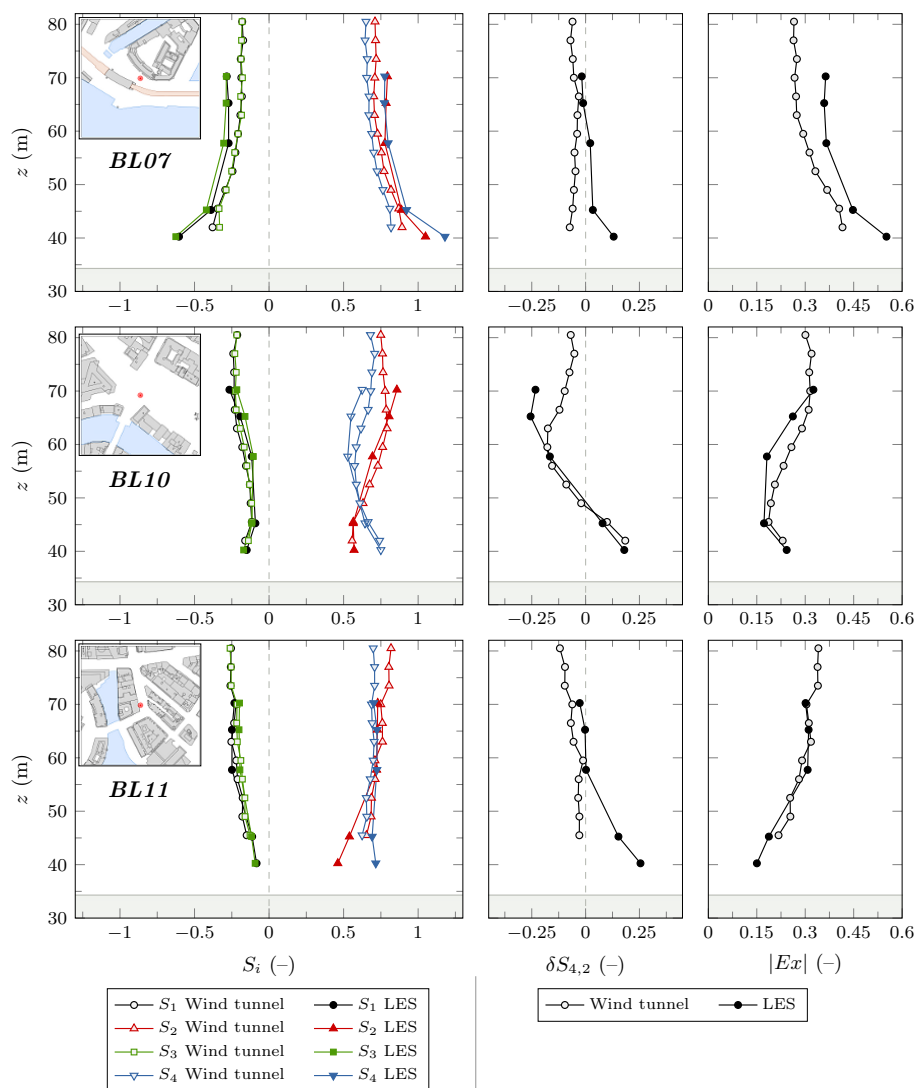


Fig. 10: Comparison of vertical profiles of wind tunnel (open symbols) and LES (filled symbols) flux fractions S_i (left), local differences between sweeps and ejections $\delta S_{4,2}$ (centre) and magnitudes of the exuberance $|Ex|$ (right) above the UCL. The grey shading indicates heights lower than H .

444 large-scale eddies [10], turbulence-resolving time-dependent simulations should be able to
 445 resolve their general characteristics.

446 At all sites ejection and sweep episodes clearly dominate the flow compared to counter-
 447 gradient fluxes, which is in agreement with other studies on surface-layer turbulence and
 448 flow characteristics within and above urban canopies, e.g. [41, 44, 37, 17, 10]. Overall, the
 449 LES captures the flux magnitudes associated with the respective quadrants. The qualitative

450 response of the momentum exchange to the local roughness characteristics strongly resem-
 451 bles the laboratory observations. Slight differences in trends are found close to roof level,
 452 where the LES predicts a dominance of downward sweep motions (Q_4) at all sites, while
 453 the laboratory flow shows a slight prevalence of ejections with the exception of location
 454 BL10. Higher up in the roughness sublayer, both the LES and the experiments show an
 455 ejection prevalence. While several of the studies cited above have documented a dominance
 456 of sweeps within and just above the canopy layer, this prevalence clearly is connected to the
 457 morphological characteristics of the analysis site and to the local flow structure. Especially
 458 in strongly heterogeneous canopies, like in this study, inferring general conclusions from
 459 local analyses is difficult.

460 At the most upstream site BL07 the largest quantitative offsets between the wind tun-
 461 nel and LES S_i profiles are observed, while qualitatively the height-dependent characteris-
 462 tics overall are well reproduced. Compared to locations further downstream here the LES
 463 and wind-tunnel flows are characterised by a larger proportion of counter-gradient fluxes at
 464 lower elevations. However, the exchange efficiency gradually increases with height as seen
 465 in the exuberance profiles $|Ex(z)|$. The smaller the exuberance magnitude, the more effi-
 466 cient the vertical turbulent momentum exchange through ejections and sweeps. The picture
 467 is different at the downtown sites BL10 and BL11, where the roughness-layer flow now is
 468 increasingly affected by three-dimensional building-induced mixing. The vertical momen-
 469 tum exchange is more efficient close to roof level (dominance of $S_2 + S_4$ over $S_1 + S_3$)
 470 and becomes less efficient at higher elevations. At the intersection site BL10 the qualitative
 471 and quantitative agreement is remarkably good. In the experiment and the LES the lowest
 472 comparison points are associated with a dominance of sweeps, while upward ejections are
 473 dominant further away from the canopy. The height profiles of $\delta S_{4,2}$ exhibit strong gradients
 474 in a region between approximately $1.3H$ to $2H$, reflecting an enhanced turbulent exchange
 475 between the flow field influenced by UCL turbulence and the upper-level flow. The largest
 476 magnitudes of Ex up to values of 0.6 are found at the lowest comparison heights at BL07.
 477 In contrast to that, at BL10 and BL11 the momentum exchange efficiency above the UCL
 478 is stronger: a change that is captured by the LES. The height ranges determined for the
 479 most efficient vertical momentum exchange are similar to those reported by Christen et al.
 480 [10] ($1.0 < z/H < 1.25$) from analyses of field measurements in a street canyon. In both
 481 the LES and the experiment, $|Ex|$ converges to a nearly constant value of about 0.3 above
 482 $2H$, indicating a Gaussian distribution of the JPDFs in the $(u'/U_{ref}, w'/U_{ref})$ plane, again in
 483 agreement with field observations [10].

484 4.1.2 Extreme events

485 The above results show that the LES provides a realistic picture of time-dependent eddy
 486 dynamics in terms of instantaneous flux contributions from episodes of downward motions
 487 of air from the roughness sublayer towards the canopy and upward bursts of low-momentum
 488 fluid at different locations throughout the city. Such events often occur intermittently with
 489 large amplitudes of the instantaneous $u'w'$ fluxes as illustrated by the JPDFs (Fig. 9) and
 490 play an important role for canopy-layer ventilation or local detrainment and re-entrainment
 491 characteristics in street canyons. The occurrence of such strong ejection and sweep episodes
 492 can be related to the propagation of large-scale coherent eddy structures at the top of the
 493 canopy layer and to the contributions of building induced vortex shedding [27, 11].

494 In order to quantify and compare the relative importance of large amplitude contribu-
 495 tions to the flux fractions, a threshold parameter (hole size) H_c is introduced in a next step

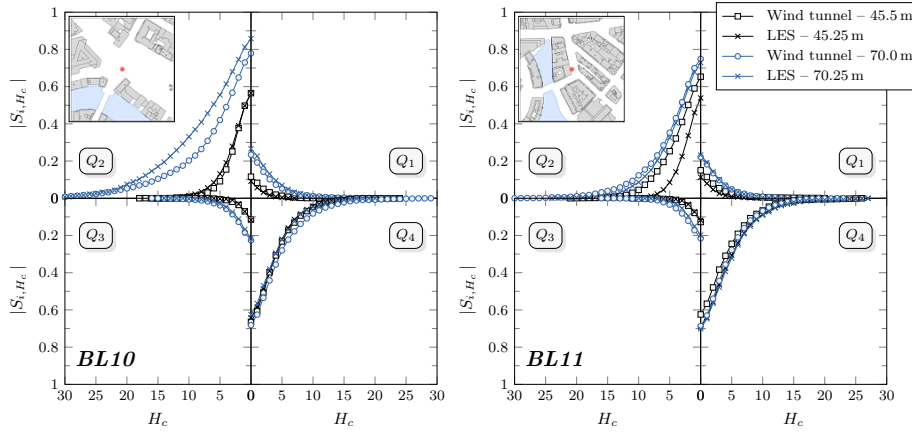


Fig. 11: The four flux fractions, $|S_{i,H_c}|$, as a function of hole size, H_c , in the wind tunnel (dots) and LES (crosses) at two comparison sites in heights of $1.3H$ (45.5 m) and $2H$ (70 m).

496 as a further constraint on the conditional averaging (see Sect. 2.2). Low-amplitude contribu-
 497 tions to the total flux are successively filtered out such that the comparatively rare but strong
 498 remaining contributions to the momentum transport can be studied.

499 Results of this analysis are shown in Fig. 11 for two heights within the roughness sub-
 500 layer: $1.3H$ (45.5 m) and $2H$ (70.25 m) at the city-centre sites BL10 and BL11. Depicted
 501 are flux fraction magnitudes, $|S_{i,H_c}|$, as a function of hole size, H_c , for which we used a
 502 maximum value of 30 to cover the entire event space. The overall agreement of the hole-size
 503 dependent flux fractions computed from wind tunnel and the LES velocity time series is
 504 very high with regard to their qualitative and quantitative evolution. At both locations the
 505 dominance of ejection and sweep contributions (Q_2 , Q_4) over the interaction quadrants (Q_1 ,
 506 Q_3) is preserved as the hole size is increased. Flux contributions from the counter-gradient
 507 Q_1 and Q_3 quadrants rapidly drop off as H_c is increased, showing that occurrences of strong
 508 flux episodes in these quadrants are very unlikely at the investigated sites. The only sig-
 509 nificant difference between the simulation and the experiment occurs at site BL10 in the
 510 Q_2 quadrant at 70.25 m. Here the LES predicts larger contributions from high-amplitude
 511 fluxes than evident in the experiment. The corresponding JPDFs (Fig. 9) indicate that this
 512 is likely connected to the occurrence of slightly larger negative streamwise velocity fluctu-
 513 ations. In the second analysis height at the same location, however, a very good qualitative
 514 and quantitative agreement of the flux-fraction evolution in all four quadrants is found. Here
 515 the prevalence of ejection motions in the upper parts of the roughness sublayer is accom-
 516 panied by significant instantaneous turbulent flux episodes at large H_c . This is also the case
 517 at location BL11, where at both heights the behaviour of $|S_{i,H_c}|$ in the experiment and the
 518 simulation is quantitatively very similar.

519 4.2 Wavelet analysis

520 In the final level of the validation study, we analyse joint time-frequency information con-
 521 tained in the wavelet coefficients $W_n(s)$ derived from velocity fluctuations as a time depen-
 522 dent extension of classic Fourier analysis. In order to study the turbulent flow with regard

523 to the occurrence of certain eddy structures, the wavelet coefficients are analysed in terms
 524 of frequency distributions of the wind tunnel and LES data. For this purpose, the wavelet
 525 transform according to Eq. (6) is conducted using the Morlet wavelet (Fig. 4) for wavelet
 526 scales corresponding to frequencies in the energy-containing spectral range, resulting in
 527 frequency-dependent time series of wavelet coefficients.

528 Fig. 12 shows frequency distributions of experimental and LES wavelet coefficients cor-
 529 responding to extraction frequencies of $f^* = fz/\bar{U} = 0.25, 0.75$ and 1.0 . These frequencies
 530 are all within the spectral peak range associated with eddies involved in turbulence produc-
 531 tion (see 1D spectra in Fig. 8). It was ensured that the fast roll-off of the LES spectra had not
 532 yet started at these frequencies, so that the information contained in the wavelet coefficients
 533 still corresponds to directly resolved scales. At these frequencies the local wavelet spectra
 534 are neither affected by aliasing at the highest frequencies nor by end effects arising from
 535 the analysis of signal portions at the beginning or end of the time series. The coefficients
 536 shown in Fig. 12 were obtained from streamwise velocity fluctuations in a height of 17.5 m
 537 ($\sim 0.5H$) at four sites corresponding to different urban settings. The time-dependent wavelet
 538 coefficients $W_n(f^*)$ were normalised by the respective standard deviations of the coefficient
 539 time series, σ_W . Results are presented using semi-logarithmic axes since we are particularly
 540 interested in the tails of the distributions, which contain information about rare, intermittent
 541 events in the flow that leave a distinct footprint in the amplitudes of the wavelet coefficients.
 542 For a quantification of the level of agreement between the experimental and LES frequency
 543 distributions the kurtosis β of the samples are derived and displayed. In order to determine
 544 deviations from a normal distribution the corresponding Gaussian curves are shown.

545 A common feature evident at all sites is that the wavelet coefficients most often exhibit
 546 small negative or positive amplitudes. The behaviour in the tails, on the other hand, is differ-
 547 ent at every site. This reflects differences in the local flow structure, but also shows a clear
 548 dependency on the frequency at which the coefficients are analysed. The smallest deviations
 549 from a normal distribution are found at the lowest frequency selected. For $f^* = 0.75$ and
 550 higher, the distributions feature heavier tails, reflecting an enhanced and intermittent activity
 551 in the flow associated with rare events and velocity bursts [16]. Deviations from the normal
 552 distribution are quantified by the respective values of β , which partially show significant
 553 offsets from the Gaussian reference ($\beta = 3$). In particular, the coefficient distributions tend
 554 to be more leptokurtic, i.e. they exhibit higher peaks and heavier tails than the normal distri-
 555 bution. This feature is seen in the experiment and the LES and similar frequency-dependent
 556 distribution characteristics can be determined at different comparison locations.

557 At all sites the LES predictions are qualitatively and quantitatively in good agreement
 558 with the wind-tunnel experiment. At the intersection position BL10, for example, both
 559 the wind-tunnel and the LES wavelet coefficient distributions exhibit extended exponen-
 560 tial tails at the two highest extraction frequencies, recognisable as a linear decay in this
 561 semi-logarithmic representation. This feature illustrates the influence of the increased sur-
 562 face roughness on the spatial scales of dominant flow structures. Quadrant analysis showed
 563 that the location above the intersection is characterised by strong and intermittent vertical
 564 momentum exchange, dominated by sweep events. Similar tail behaviour is also detected
 565 at other comparison locations, notably at the river location BL04 ($f^* = 1.0$). The kurtosis
 566 values indicate that the LES distributions have a tendency to be slightly more leptokurtic
 567 than the reference at $f^* = 1.0$, i.e. high amplitude oscillations in the wavelet coefficients
 568 are occurring more frequently than in the reference experiment. This could be a result of
 569 the proximity to the steep drop-off observed in the energy spectra. The increased level of
 570 intermittency could be an indication for the increased influence of the grid cut-off in the
 571 transition region between resolved and unresolved turbulence.

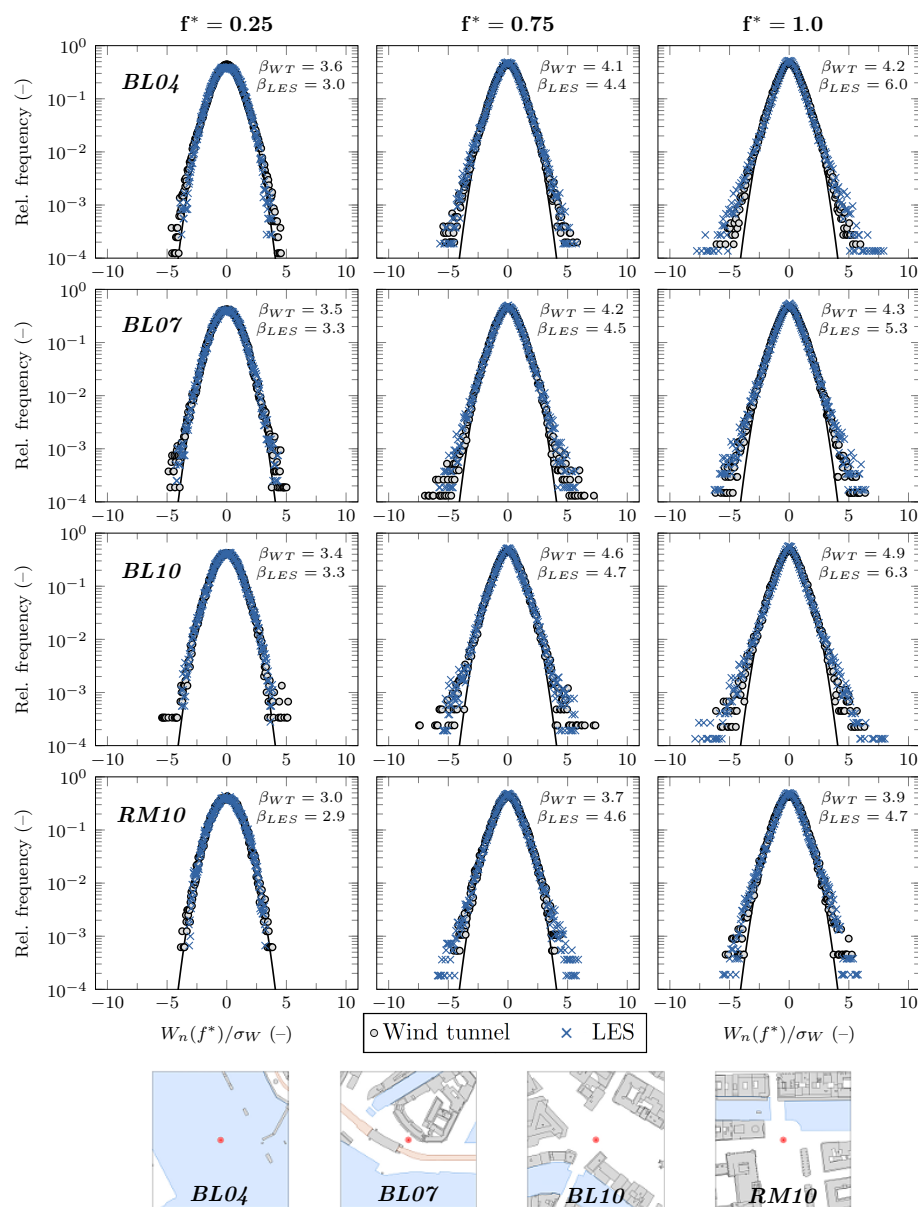


Fig. 12: Comparison of wind tunnel (dots) and LES (crosses) frequency distributions of Morlet wavelet coefficients derived from streamwise velocity fluctuations at four locations in a height of $0.5H$ (17.5 m). The distributions correspond to scaled frequencies of $f^* = f_z/\bar{U} = 0.25$ (left), 0.75 (centre) and 1.0 (right). The black lines show the corresponding Gaussian distributions.

572 **5 Discussion and conclusions**

573 5.1 Evaluation of the Hamburg test case

574 The Hamburg validation test case showed that the quality of LES can be assessed in detail by not only focusing on comparisons of low-order statistics, but by taking into account
 575 the time-dependent nature of the problem. Following the multi-level validation concept proposed in part I we established that the tested LES code, FAST3D-CT, provides a realistic
 576 representation of mean flow and turbulence statistics in the urban roughness sublayer. This assessment was further substantiated by a direct comparison of time series in terms
 577 of frequency distributions, showing that the LES accurately reproduces complex geometry-induced flow patterns, e.g. flow-switching events reflected in bimodal velocity histograms.
 578 In part II presented here we have extended the analysis by examining the underlying flow structure in detail with regard to time-dependent flow statistics and flow features associated
 579 with energy and flux-dominating eddies that are directly resolved by the LES.
 580
 581
 582
 583
 584

585 5.1.1 Eddy scale and flow pattern analysis

586 Compared to small-scale turbulence structures, energy and flux-dominating large-scale vortices occur less frequently. The representativity of associated statistical measures thus is
 587 strongly coupled to the duration of the signal, i.e. to the measurement or simulation time. Computational costs and computing time restrictions often result in the fact that there is
 588 a significant difference in LES signal lengths compared to the reference data, as was the case in our example study. While in this case the inherent uncertainty of low-order statistics
 589 obtained from the longer wind tunnel and shorter LES time series ($T_{exp} = 16.5$ h and $T_{les} = 6.5$ h) is negligible compared to the experimental reproducibility, this may not be
 590 true for more sensitive parameters. An example is S_{i,H_c} , which measures the relevance of extreme flux episodes associated with large, infrequently occurring eddies. The magnitude
 591 of this effect can for example be assessed based on the longer experimental data record. Repeating the hole-size analysis of Sect. 4.1.2 with a wind-tunnel time series that is shorter
 592 by a factor of $T_{exp}/T_{les} = 2.5$ showed non-negligible differences in the flux fractions of the $Q_{2,4}$ quadrants that are associated with coherent eddies. The larger the number of energy-
 593 dominating structures that have passed the sensor, the more robust are statistics associated with this eddy class. This has to be kept in mind when evaluating the agreement between
 594 LES and experiment.
 595
 596
 597
 598
 599
 600
 601
 602

603 *Eddy statistics* Since reference data are still predominantly available in terms of single-point measurements, as was also the case in the test study, the focus should be on comparisons of
 604 dominant turbulence *time scales* and *temporal* autocorrelations to learn about the structure of the flow. In general, this can be extended into spatial correlation analyses given reference
 605 data of sufficient spatial resolution. For the model tested here, we found that the height dependence of integral time scales of the three velocity components overall is well reproduced
 606 in the simulation. Given the complexity of the canopy-layer flow field and the general sensitivity of measures based on correlations, this underlines the general suitability of the tested
 607 code for urban aerodynamics simulations.
 608
 609
 610
 611

612 Analysing spectral energy densities allows the evaluation of contributions from eddies of different size to the local flow variance. With LES it is of particular interest to investigate
 613 up to what frequency range turbulence structures are directly resolved, which can be readily determined by the characteristic fast roll-off of the spectra as a result of the grid truncation.
 614
 615

616 In the Hamburg LES, the roll-off occurred in the transition region between the turbulence
617 production range and the inertial subrange. Within the UCL, a scale decrease of the produc-
618 tion range eddies is clearly reflected in the wind-tunnel spectra as a shift of the energy peaks
619 towards higher frequencies. Given this eddy size reduction, the uniform grid resolution of
620 2.5 m in combination with the implicit dissipation scheme causes the LES to be at the verge
621 of being a “very large-eddy simulation” within the UCL. Despite this resolution limitation,
622 at the majority of comparison sites the spectral shapes in the energy-dominating frequency
623 range agree well with the experimental targets. This applies to frequency ranges associated
624 with the spectral peak region and to the distribution of energy among the largest eddies in
625 the flow, demonstrating that the LES accurately resolves turbulence that dominate the flow
626 in terms of turbulence kinetic energy and turbulent mixing.

627 *Eddy structure and flow dynamics* Within the atmospheric surface layer, turbulence is highly
628 three-dimensional, particularly so within the urban canopy layer. Whether eddy-resolving
629 simulation techniques are resolving the structure of turbulence in a realistic way can be
630 analysed by means of structure identification methods, e.g. quadrant analysis, as done for the
631 Hamburg test case. We showed that the efficiency of vertical momentum exchange, which is
632 a quantity of interest for street-canyon ventilation or vertical detrainment, can be used as a
633 quality control measure for the simulation. In the test case, for example, the LES produced
634 momentum flux characteristics that are in agreement with the reference case regarding the
635 local dominance of upward or downward motions associated with coherent eddy structures
636 (gradient-type motions). Carrying out these comparisons at structurally different flow lo-
637 cations allows the study of changes in the characteristics of flux events in response to the
638 underlying roughness. By introducing a hole-size constraint to the conditional re-sampling
639 process, the occurrence of flux contributions linked to infrequent, high-amplitude events
640 in the flow was evaluated. The good agreement of the H_c -dependent flux fractions shows
641 that the LES realistically represents the local dominance of downward sweeps of high-
642 momentum fluid towards the UCL and upward ejections of low-momentum fluid into the
643 upper parts of the roughness sublayer.

644 Extending the classic Fourier analysis, the time-dependent flow structure can be com-
645 pared in a joint time-frequency framework. Scale-dependent analyses of the turbulent flow
646 field based on wavelet transform methods offer strong potential here, and in the Hamburg
647 test case revealed a structural agreement of the time-dependent experimental and LES flows.
648 The comparison of frequency distributions of wavelet coefficients extracted at energetically
649 dominant frequencies reveal occurrence characteristics of rare but energetically significant
650 turbulence episodes. Depending on the extraction frequency and the comparison location,
651 the wavelet coefficient PDFs can feature heavy tails, which is an indication for an increased
652 level of intermittency in the flow. By comparing the kurtosis values associated with the dis-
653 tributions the level of agreement can be quantified.

654 5.1.2 Model accuracy

655 Applying the proposed validation strategy showed that FAST3D-CT provides realistic and
656 reliable information about urban turbulence with regard to geometry-induced mean and in-
657 stantaneous flow features. Despite the overall strong performance of FAST3D-CT some
658 systematic discrepancies were identified. In part I we discussed how the grid resolution of
659 2.5 m in combination with the computational representation of buildings by simple grid
660 masking negatively affected the comparison, particularly in narrow street canyons. Spectral
661 analyses performed in part II revealed how the grid resolution also affected the resolution

662 potential of flow structures in the implicit LES. Although a grid-resolution of 2.5 m should
663 make it possible to resolve at least one frequency decade of inertial subrange turbulence,
664 the FCT-scheme handling the numerical dissipation in the model in its current configuration
665 seemed to contribute to an enhanced energy loss, identifiable in the turbulence spectra. In
666 general it can be expected that this also has an effect on mean flow and turbulence statistics,
667 adding to the other sources of discrepancies identified before. Within the UCL, FAST3D-CT
668 in this study only fully resolved eddies in the production range, which is characteristic for
669 a very large-eddy simulation. The grid resolution also affected the overall comparability of
670 the data due to spatial offsets between comparison locations in the experiment and the LES.
671 Seemingly marginal height differences in the order of 0.25 m can have a significant influence
672 on the results in regions of strong flow gradients. The same is true for spatial offsets in the
673 (x,y) plane in strongly heterogeneous flow situations or near building walls. Re-running the
674 Hamburg case with a more detailed representation of buildings, e.g. based on unstructured
675 meshes or immersed boundary methods, would certainly lead to a better understanding of
676 some of the discrepancies determined here. It can be expected that there will be improve-
677 ments particularly at comparison points located in narrow streets. The same can be expected
678 of refinements of the grid resolution in connection with the FCT-scheme, and improvements
679 of the inflow modelling. In order to disentangle these overlapping sources of inaccuracy and
680 to determine the effects of a better reproduction of low-frequency inertial range eddies, the
681 resolution would need to be increased to 1 m or below. However, these improvements in-
682 evitably lead to higher computational costs. For example, doubling the grid resolution will
683 result in a sixteen-fold increase in run time. Alternatively, the simulation could be re-run in
684 a much smaller domain, making the increase in grid resolution affordable, while possibly
685 also being able to explore more accurate buildings representation techniques.

686 5.2 Conclusions and outlook

687 The work presented here was motivated by the lack of proportion between the increasing
688 use of eddy-resolving CFD methods like LES for micro-meteorological and environmental
689 fluid mechanics applications and the level of scrutiny that is commonly applied to vali-
690 date the simulation results. Based on the example of highly complex urban boundary-layer
691 flow we showed that through a rigorous validation against qualified reference data based
692 on model-specific tests, the suitability of time-dependent, turbulence-resolving simulations
693 for their intended use can be documented, and the bounds of uncertainty in the results can
694 be quantified. With well-established signal analysis methods and by means of suitable and
695 quality-controlled reference data, a high level of detail can be incorporated into the vali-
696 dation of LES. The information gained by far exceeds what can be learned based on the
697 traditional approach of comparing mean flow and turbulence statistics. By applying the se-
698 quence of analysis methods to the Hamburg flow simulation we were able to validate, for
699 example, the representation of

- 700 – Velocity fluctuations in response to local flow structure
- 701 – Time scales associated with dominant turbulent eddies
- 702 – Distribution of energy among flow structures of different size
- 703 – Turbulent exchange efficiency associated with different eddy structures
- 704 – Contribution of extreme events to local turbulent exchange characteristics
- 705 – Flow intermittency captured in time-dependent energy spectra.

706 While the validation method was tested based on the specific case of urban turbulence,
707 it can also be applied to validate other types of eddy-resolving boundary-layer simulations,

708 for example flow within and above plant canopies or above a uniform roughness (e.g. only
709 prescribed through the roughness length). Similar validation concepts based on time-series
710 analyses can also be applied to validate simulations of scalar dispersion or heat exchange.
711 The methods can also be applied to other types of turbulence-resolving simulations to study
712 local-scale problems like detached eddy simulation or direct numerical simulations, but also
713 to high-resolution meteorological models ($O(10 - 100 \text{ m})$) applied to study problems in
714 which length-scales of energy-dominating eddies scale with the boundary-layer depth.

715 The study showed that experiments in boundary-layer wind tunnels with full control over
716 mean inflow and boundary conditions, flexibility in the geometric design of the test case and
717 measurement repeatability offer great potential for model validation. However, wind-tunnel
718 experiments themselves are models with strong geometric and physical abstractions. The
719 potential, for example, to realistically model effects like differential heating on surfaces, an-
720 thropogenic heating, evapo-transpiration from vegetation, strong convection or stable strat-
721 ification in wind tunnels is limited. Therefore, ideally laboratory studies are accompanied
722 by full-scale field experiments and *vice versa*. While only the latter can capture the full
723 complexity of natural atmospheric flows, the former allows the systematic study of relevant
724 processes in isolation. Urban studies for which field and wind-tunnel data are available and
725 in the past were used for comprehensive model validation include for example the DAPPLE
726 experiment in central London [62], the MUST experiment in the Utah desert [5,47] or the
727 Joint Urban 2003 campaign in Oklahoma City [24].

728 LES is increasingly applied to real-life problems of practical concern and quality as-
729 surance is becoming more and more crucial. Community-wide activities are now needed
730 in order to streamline model validation efforts. Micro-meteorology and wind engineering
731 communities have demonstrated before that multi-national, multi-institutional activities for
732 the harmonisation of validation approaches for flow in urban environments are feasible. The
733 COST Actions 732 [7,48,21] and ES1006 [58] are encouraging examples of how exchange
734 between experimentalists and modellers can result in broadly accepted model quality stan-
735 dards, best-practice simulation protocols and validation guidelines for flow and dispersion
736 models applied to problems on the urban micro-scale. Similar activities need to be pursued
737 for LES, involving model developers and users as well as field and laboratory experimental-
738 ists. For micro-meteorological and environmental fluid mechanics applications in the near-
739 surface boundary layer, the joint formulation of validation guidelines need to stress the role
740 of advanced turbulence analysis methods and flow structure recognition techniques, and the
741 need for standards regarding quality and quantity requirements for reference data.

742 **Acknowledgements** The numerical simulations with the LES code FAST3D-CT were carried out at the
743 Laboratories for Computational Physics and Fluid Dynamics of the U.S. Naval Research Laboratory in Wash-
744 ington D.C., USA. The authors wish to express their thanks to Jay Boris, Mi-Young Obenschain and other
745 collaborators there. Further thanks is given to colleagues at the Environmental Wind Tunnel Laboratory at the
746 University of Hamburg. Financial funding by the German Federal Office of Civil Protection and Disaster As-
747 sistance as well as by the Ministry of the Interior of the City of Hamburg within the "Hamburg Pilot Project" is
748 gratefully acknowledged (BBK research contract no. BBK III.1-413-10-364). Parts of the wind-tunnel model
749 construction were financially supported by the KlimaCampus at the University of Hamburg.

750 References

- 751 1. Addison, P.S.: The illustrated wavelet transform handbook: Introductory theory and applications in sci-
752 ence, engineering, medicine and finance. Institute of Physics Publishing, London (2002)
- 753 2. Adrian, R.J.: Hairpin vortex organization in wall turbulence. *Phys Fluids* **19**, 041,301 (2007)

- 754 3. Basu, S., Vinuesa, J.F., Swift, A.: Dynamic les modeling of a diurnal cycle. *J Appl Meteorol Climatol*
755 **47**, 1156–1174 (2008)
- 756 4. Beare, R.J., Macvean, M.K., Holtslag, A.A.M., Cuxart, J., Esau, I., Golaz, J.C., Jimenez, M.A., Khairout-
757 dinov, M., Kosovic, B., Lund, D.L.T.S., Lundquist, J.K., McCabe, A., Moene, A.F., Noh, Y., Raasch, S.,
758 Sullivan, P.: An intercomparison of large-eddy simulations of the stable boundary layer. *Bound-Lay*
759 *Meteorol* **118**, 247–272 (2006)
- 760 5. Biltoft, C.A.: Customer report for MOck Urban Setting Test (MUST). Tech. Rep. WDTC-FR-01-121,
761 West Desert Test Center, U.S. Army Dugway Proving Ground, Dugway (UT), USA (2001)
- 762 6. Boppana, V.B.L., Xie, Z.T., Castro, I.P.: Large-eddy simulation of dispersion from surface sources in
763 arrays of obstacles. *Bound-Lay Meteorol* **135**, 433–454 (2010)
- 764 7. Britter, R., Schatzmann, M. (eds.): Model evaluation guidance and protocol document. COST Action
765 732. University of Hamburg, Germany (2007b)
- 766 8. Chlond, A., Böhringer, O., Auerswald, T., Müller, F.: The effect of soil moisture and atmospheric condi-
767 tions on the development of shallow cumulus convection: A coupled large-eddy simulation land surface
768 model study. *Meteorol Z* **23**(5), 491–510 (2014)
- 769 9. Chow, F.K., Weigel, A.P., Street, R.L., Rotach, M.W., Xue, M.: High-resolution large-eddy simulations
770 of flow in a steep alpine valley. Part I: Methodology, verification, and sensitivity experiments. *J Appl*
771 *Meteorol Climatol* **45**, 63–86 (2006)
- 772 10. Christen, A., van Gorsel, E., Vogt, R.: Coherent structures in urban roughness sublayer turbulence. *Int J*
773 *Climatol* **27**, 1955–1968 (2007)
- 774 11. Coceal, O., Dobre, A., Thomas, T.G.: Unsteady dynamics and organized structures from DNS over an
775 idealized building canopy. *Int J Climatol* **27**, 1943–1953 (2007)
- 776 12. Conzemius, R., Fedorovich, E.: Bulk models of the sheared convective boundary layer: Evaluation
777 through large eddy simulations. *J Atmos Sci* **64**, 786–807 (2007)
- 778 13. Cooley, J.W., Tukey, J.W.: An algorithm for the machine calculation of complex Fourier series. *Math*
779 *Comput* **19**, 297–301 (1965)
- 780 14. Deardorff, J.W.: A numerical study of three-dimensional turbulent channel flow at large Reynolds num-
781 bers. *J Fluid Mech* **41**, 453–480 (1970)
- 782 15. Farge, M.: Wavelet transforms and their application to turbulence. *Annu Rev Fluid Mech* **24**, 395–457
783 (1992)
- 784 16. Farge, M., Schneider, K., Pannekoucke, O., Nguyen van yen, R.: Multiscale representations. In: H.J.S.
785 Fernando (ed.) *Handbook of Environmental Fluid Dynamics*, vol. II: Systems, Pollution, Modeling, and
786 Measurements. CRC Press (2012)
- 787 17. Feddersen, B.: Wind tunnel modelling of turbulence and dispersion above tall and highly dense urban
788 roughness. Ph.D. thesis, Swiss Federal Institute of Technology (2005). Diss. ETH No. 15934
- 789 18. Feigenwinter, C., Vogt, R.: Detection and analysis of coherent structures in urban turbulence. *Theor*
790 *Appl Climatol* **81**, 219–230 (2005)
- 791 19. Finnigan, J.J.: Turbulence in plant canopies. *Annu Rev Fluid Mech* **32**, 519–571 (2000)
- 792 20. Fischer, R.: Entwicklung eines problemorientierten Software-Pakets zur automatisierten Aufbereitung,
793 Analyse und Dokumentation von im Windkanal produzierten Daten zur LES-Validierung. Ph.D. thesis,
794 University of Hamburg (2011). In German
- 795 21. Franke, J., Hellsten, A., Schlünzen, K.H., Carissimo, B.: The COST 732 Best Practice Guideline for
796 CFD simulation of flows in the urban environment: a summary. *Int J Environ Pollut* **44**, 419–427 (2011)
- 797 22. Grossmann, A., Morlet, J.: Decomposition of Hardy functions into square integrable wavelets of constant
798 shape. *SIAM J Math Anal* **15**, 723–736 (1984)
- 799 23. Grossmann, A., Morlet, J., Paul, T.: Transforms associated to square integrable group representations I:
800 General results. *J Math Anal* **26**, 2473–2479 (1985)
- 801 24. Harms, F., Leitl, B., Schatzmann, M., Patnaik, G.: Validating LES-based flow and dispersion models. *J*
802 *Wind Eng Ind Aerod* **99**, 289–295 (2011)
- 803 25. Kaimal, J.C., Wyngaard, J.C., Izumi, Y., Coté, O.R.: Spectral characteristics of surface-layer turbulence.
804 *Q J Roy Meteor Soc* **98**, 563–589 (1972)
- 805 26. Kaiser, G.: *A Friendly Guide to Wavelets*, first edn. Birkhäuser Boston (1994)
- 806 27. Kanda, M., Moriawaki, R., Kasamatsu, F.: Large-eddy simulation of turbulent organized structures within
807 and above explicitly resolved cube arrays. *Bound-Lay Meteorol* **112**, 343–368 (2004)
- 808 28. Letzel, M.O.: Urban large-eddy simulation (LES), Advanced computational fluid dynamics for urban
809 climatic maps. In: E. Ng, C. Ren (eds.) *The Urban Climatic Map: A Methodology for Sustainable Urban*
810 *Planning*, chap. 32, pp. 421–428. Routledge, New York (2015)
- 811 29. Letzel, M.O., Raasch, S.: Large eddy simulation of thermally induced oscillations in the convective
812 boundary layer. *J Atmos Sci* **60**, 2328–2341 (2003)
- 813 30. Lilly, D.K.: The representation of small-scale turbulence in numerical simulation experiments. In: H.H.
814 Goldstine (ed.) *Proceedings of the IBM Scientific Computing Symposium on Environmental Sciences*,
815 pp. 195–210. Yorktown Height, New York (1967)

- 816 31. Lumley, J.L., Panofsky, H.A.: *The Structure of Atmospheric Turbulence*. Interscience Publishers, New
817 York (1964)
- 818 32. Meneveau, C.: Analysis of turbulence in the orthonormal wavelet representation. *J Fluid Mech* **232**,
819 469–520 (1991)
- 820 33. Michioka, T., Chow, F.K.: High-resolution large-eddy simulation of scalar transport in atmospheric
821 boundary layer flow over complex terrain. *J Appl Meteorol Climatol* **47**, 3150–3169 (2008)
- 822 34. Morlet, J.: Sampling theory and wave propagation. In: *Proceedings of the 51st Annual International*
823 *Meeting of the Society of Exploration Geophysicists*. Los Angeles (CA), USA (1981)
- 824 35. Nieuwstadt, F.T.M., Mason, P.J., Moeng, C.H., Schumann, U.: Large-eddy simulation of the convective
825 boundary layer: A comparison of four computer codes. In: F. Durst, B.E. Launder, R. Friedrich, F.W.
826 Schmidt (eds.) *Turbulent Shear Flows 8*, pp. 343–367. Springer (1993)
- 827 36. Nobach, H., Tropea, C., Cordier, L., Bonnet, J.P., Delville, J., Lewalle, J., Farge, M., Schneider, K.,
828 Adrian, R.J.: Review of some fundamentals of data processing. In: C. Tropea, A.L. Yarin, J.F. Foss
829 (eds.) *Springer Handbook of Experimental Fluid Mechanics, Part D: Analysis and Post-Processing of*
830 *Data*. Springer (2007)
- 831 37. Oikawa, S., Meng, Y.: Turbulence characteristics and organized motion in a suburban roughness sublayer.
832 *Bound-Lay Meteorol* **74**, 289–312 (1995)
- 833 38. O'Neill, P.L., Nicolaides, D., Honnery, D., Soria, J.: Autocorrelation functions and the determination
834 of integral length with reference to experimental and numerical data. In: *Proceedings of the 15th Aus-*
835 *tralasian Fluid Mechanics Conference*. The University of Sydney, Sydney, Australia (2004)
- 836 39. Patnaik, G., Boris, J.P., Grinstein, F.F., Iselin, J.P., Hertwig, D.: Large scale urban simulations with
837 FCT. In: D. Kuzmin, R. Löhner, S. Turek (eds.) *Flux-Corrected Transport: Principles, Algorithms, and*
838 *Applications*, Scientific Computing, second edn., pp. 91–117. Springer (2012)
- 839 40. Patnaik, G., Grinstein, F.F., Boris, J.P., Young, T.R., Parmhed, O.: Large-scale urban simulations. In: F.F.
840 Grinstein, L.G. Margolin, W.J. Rider (eds.) *Implicit Large Eddy Simulation: Computing Turbulent Fluid*
841 *Dynamics*. Cambridge University Press (2007)
- 842 41. Raupach, M.R.: Conditional statistics of Reynolds stress in rough-wall and smooth-wall turbulent bound-
843 ary layers. *J Fluid Mech* **108**, 363–382 (1981)
- 844 42. Raupach, M.R., Thom, A.S.: Turbulence in and above plant canopies. *Ann Rev Fluid Mech* **13**, 97–129
845 (1981)
- 846 43. Robinson, S.K.: Coherent motions in the turbulent boundary layer. *Annu Rev Fluid Mech* **23**, 601–639
847 (1991)
- 848 44. Rotach, M.W.: Turbulence close to a rough urban surface - Part I: Reynolds stresses. *Bound-Lay Mete-*
849 *orol* **65**, 1–28 (1993)
- 850 45. Rotach, M.W.: Profiles of turbulence statistics in and above an urban street canyon. *Atmos Environ* **29**,
851 1473–1486 (1995)
- 852 46. Roth, M.: Review of atmospheric turbulence over cities. *Q J Roy Meteor Soc* **126**, 941–990 (2000)
- 853 47. Sabatino, S.D., Buccolieri, R., Olesen, H.R., Ketzler, M., Berkowicz, R., Franke, J., Schatzmann, M.,
854 Schlunzen, K., Leitl, B., Britter, R., Borrego, C., Costa, A., Castelli, S., Reisin, T., Hellsten, A., Saloranta,
855 J., Moussiopoulos, N., Barmpas, F., Brzozowski, K., Goricsan, I., Balczó, M., Bartzis, J., Efthimiou, G.,
856 Santiago, J., Martilli, A., Piringer, M., Baumann-Stanzer, K., Hirtl, M., Baklanov, A., Nuterma, R.,
857 Starchenko, A.: COST 732 in practice: the MUST model evaluation exercise. *Int J Environ Pollut* **44**,
858 403–418 (2011)
- 859 48. Schatzmann, M., Britter, R.: Quality assurance and improvement of micro-scale meteorological models.
860 *Int J Environ Pollut* **44**, 139–146 (2011)
- 861 49. Schlegel, F., Stiller, J., Bienert, A., Maas, H.G., Queck, R., Bernhofer, C.: Large-eddy simulation of
862 inhomogeneous canopy flows using high resolution terrestrial laser scanning data. *J Fluid Mech* **142**,
863 223–243 (2012)
- 864 50. Schumann, U.: Subgrid scale model for finite difference simulations of turbulent flows in plane channels
865 and annuli. *J Comput Phys* **18**, 376–404 (1975)
- 866 51. Seifert, A., Heus, T., Pincus, R., Stevens, B.: Large-eddy simulation of the transient and near-equilibrium
867 behavior of precipitating shallow convection. *J Adv Model Earth Sy* **7**, 1918–1937 (2015)
- 868 52. Shaw, R.H., Schumann, U.: Large-eddy simulation of turbulent flow above and within a forest. *Bound-*
869 *Lay Meteorol* **61**(1), 47–64 (1992)
- 870 53. Shaw, R.H., Tavangar, J., Ward, D.P.: Structure of Reynolds stress in a canopy. *J Clim Appl Meteorol*
871 **22**, 1922–1931 (1983)
- 872 54. Smagorinsky, J.: General circulation experiments with the primitive equations: I. The basic experiment.
873 *Mon Weather Rev* **91**, 99–164 (1963)
- 874 55. Stull, R.B.: *An Introduction to Boundary Layer Meteorology*. Kluwer Academic Publishers, Dordrecht
875 (1988)
- 876 56. Torrence, C., Compo, G.P.: A practical guide to wavelet analysis. *B Am Meteorol Soc* **79**, 61–78 (1998)

- 877 57. Townsend, A.A.: *The Structure of Turbulent Shear Flow*. Cambridge University Press, Cambridge (1956)
- 878 58. Trini Castelli, S., Baumann-Stanzer, K., Leiti, B., Milliez, C.M., Berbekar, E., Rakai, A., Fuka, V., Hell-
- 879 sten, A., Petrov, A., Efthimiou, G., Andronopoulos, S., Tinarelli, G., Tavares, R., Armand, P., Gariazzo,
- 880 C., Jurcakova, K., Gašparac, G.: Evaluation of local-scale models for accidental releases in built envi-
- 881 ronments: Results of the modelling exercises in cost action es1006. In: G.D. Steyn, N. Chaumerliac
- 882 (eds.) *Air Pollution Modeling and its Application XXIV*, pp. 497–502. Springer International Publishing
- 883 (2016)
- 884 59. Wallace, J.M.: Quadrant analysis in turbulence research: history and evolution. *Annu Rev Fluid Mech*
- 885 **48**, 131–158 (2016)
- 886 60. Wallace, J.M., Eckelmann, H., Brodkey, R.: The wall region in turbulent shear flow. *J Fluid Mech* **53**,
- 887 39–48 (1972)
- 888 61. Willmarth, W.W., Lu, S.S.: Structure of the Reynolds stress near the wall. *J Fluid Mech* **55**, 65–92 (1972)
- 889 62. Wood, C.R., Barlow, J.F., Belcher, S.E., Dobre, A., Arnold, S.J., Balogun, A.A., Lingard, J.J.N., Smal-
- 890 ley, R.J., Tate, J.E., Tomlin, A.S., Britter, R.E., Cheng, H., Martin, D., Petersson, F.K., Shallcross, D.E.,
- 891 White, I.R., Neophytou, M.K., Robins, A.G.: Dispersion experiments in central London: The 2007 DAP-
- 892 PLE project. *B Am Meteorol Soc* **90**, 955–969 (2009)
- 893 63. Wyngaard, J.C., Coté, O.R.: Cospectral similarity in the atmospheric surface layer. *Q J Roy Meteorol*
- 894 *Soc* **98**, 590–603 (1972)
- 895 64. Yaglom, A.M.: *Correlation Theory of Stationary and Related Random Functions I: Basic Results*.
- 896 Springer (1987)
- 897 65. Yue, W., Parlange, M.B., Meneveau, C., Zhu, W., van Hout, R., Katz, J.: Large-eddy simulation of plant
- 898 canopy flows using plant-scale representation. *Bound-Lay Meteorol* **124**, 183–203 (2007)